RSC Advances

PAPER

View Article Online
View Journal | View Issue

Cite this: *RSC Adv.*, 2025, **15**, 12834

Novel lead-free bismuth-based perovskite-like $(BrC_5H_{13}N)_3Bi_2Br_9$: synthesis, structural investigations and optoelectronic properties†

Yassine Ben Elhaj,[a] Fadhel Hajlaoui,*[a] Karim Karoui,[bc] Magali Allain,[d] Nicolas Mercier,[d] Erika Kozma,[e] Chiara Botta[e] and Nabil Zouari[a]

Lead-free organic–inorganic hybrid perovskites have attracted increasing attention owing to their advantages of reduced toxicity, photo-detectability, switchable dielectric device application, ferroelectric properties and distinctive optical characteristics. Despite their promising features, the chemical engineering of hybrid perovskites remains a challenge, as identifying the appropriate strategies is essential to achieve the desired properties such as controlled bandgap energy and phase transition behaviours. Numerous approaches have been explored to optimize these characteristics. In this study, we employed halogenation of the organic component as a targeted strategy to enhance the stability and performance of hybrid perovskite materials. This approach enabled the successful synthesis of a non-centrosymmetric halobismuthate $(BrC_5H_{13}N)_3Bi_2Br_9$ compound ($BrC_5H_{13}N^+$: (2-bromoethyl) trimethylammonium), which exhibited excellent optic and electric properties and crystallized in the non-polar $P2_12_12_1$ space group. The inorganic framework was precisely arranged with $[Bi_2Br_9]^{3-}$ polyhedra that were face-shared and separated by organic cations, resulting in an $A_3B_2X_9$-type structure. Additionally, the compound $(BrC_5H_{13}N)_3Bi_2Br_9$ possessed an indirect band gap of 2.58 eV, which suggests this material's semiconductor character. Photoluminescence (PL) studies revealed that the compound exhibited a broad band emission at about 730 nm. The electrical properties as a function of frequencies and temperatures showed the contribution of the grain and grain boundary to conduction, and AC conductivity confirmed the semiconductor behaviour. The activation energy suggested the combination of ionic and electronic conduction. These findings enrich the understanding on the behaviour of $A_3B_2X_9$-type low-dimensional hybrids and holds promise in extending the application of lead-free hybrids to the field of ferroelectric, electric and optic materials.

Received 10th March 2025
Accepted 7th April 2025

DOI: 10.1039/d5ra01714a

rsc.li/rsc-advances

Introduction

Hybrid perovskites have attracted significant attention due to their impressive features such as semi-conductivity, large absorption coefficients and long carrier lifetime, making them applicable in the fields of solar cells, light-emitting diodes, and gas sensors.[1–3] Their capacity to combine the characteristics of organic and inorganic components into a single molecule has made research on these materials one of the most important and promising areas of study.[4–7] The interest in these types of materials has increased in the last decade owing to the fascinating performance of hybrid perovskites in several fields. For example, a power conversion efficiency of 25.8% was achieved using α-formamidinium lead tri-iodide (FAPbI3) perovskite,[8] an external quantum efficiency approaching 30% was achieved for the green light-emitting diode using $[FA_{0.7}MA_{0.1}GA_{0.2}]_{0.87}Cs_{0.13}PbBr_3$ (FA: formamidinium; GA: guanidinium; MA: methylammonium),[9] and a capability over 1 ppm was achieved in detecting ammonia gas using $CH_3NH_3PbI_3$.[10]

Separated by layers of organic cations, the perovskite crystals are made up of inorganic BX_6 octahedra, where "X" is a halogen atom and "B" is a metal ion, and they can form 3D networks, 2D layers, 1D chains or discrete clusters.[11–13] Although these layered hybrid materials are similar to inorganic perovskites with the formula ABX_3, hybrid perovskites offer more degrees of freedom when aliphatic and aromatic spacers with soft organic tails, acting as templating agents, are positioned in cavities encircled

[a]*Laboratoire Physico-chimie de l'Etat Solide, Département de Chimie, Faculté des Sciences de Sfax, Université de Sfax, B. P. 1171, 3000 Sfax, Tunisia. E-mail: fadhelh83@yahoo.fr*

[b]*Laboratoire des Caractérisations Spectroscopiques et Optique des Matériaux, Faculté des Sciences de Sfax, Université de Sfax, B.P. 1171, 3000 Sfax, Tunisia*

[c]*GREMAN UMR 7347-CNRS, CEA, INSACVL, University of Tours, Blois, France*

[d]*MOLTECH Anjou, UMR-CNRS 6200, Univ Angers, 2 Bd Lavoisier, 49045 Angers, France*

[e]*Istituto di Scienze e Tecnologie Chimiche "G. Natta" (SCITEC), CNR, Via A. Corti 12, 20133 Milano, Italy*

† Electronic supplementary information (ESI) available. CCDC 2429859. For ESI and crystallographic data in CIF or other electronic format see DOI: https://doi.org/10.1039/d5ra01714a

by octahedra anionic groups or between neighbouring layered metal halides.[14] Organic molecules and inorganic frameworks can combine to provide a wide range of structural variations with better characteristics by increasing structural flexibility and polarizability.[15] Perhaps the best-known characteristic of hybrid perovskites is that their physical properties can be tuned widely. Crucially, their structural phase transitions are the source of many of these properties. For instance, the bandgap energy (E_g) of the hybrid perovskites is crucial for the semiconductor domain application. The halogen's p-orbitals play a significant role in the optical transition, which primarily determines the E_g value. Additionally, the substantial effect of halogen substitution on $CH_3NH_3PbX_3$ (X = Cl, Br, and I) was investigated by C. Tablero Crespo, who demonstrated that such substitution significantly influences the perovskite's bandgap energy value.[16] However, even though the A-site has little effect on the electronic band structure, it can affect the phase transition and stability. Since the structure of halogenated hybrid perovskites can support a variety of organic amine cations, the size, shape and valence of these cations determine their crystal symmetries and guest–host interactions, leading to additional structural freedom and associated complex phase transition behavior.[17–19] For example, by regulating the quantity of Cs in the A-site, B. Dridi Rezgui *et al.* were able to support the stability of the α-phase of $FA_{1-x}Cs_xPbI_3$ (FA = formamidinum).[20] Additionally, another study shows that the phase transition temperature can be affected by the Cs doping of $FAPbI_3$, and that the doped compound $FA_{0.85}Cs_{0.15}PbI_3$ demonstrated better device stability and performance in comparison to their $FAPbI_3$ counterparts.[21] Some other studies concentrate on adding a halogen on the A-site, which can provide additional stability and regulate the band gap, starting from the fact that the halogen can have a significant impact on the gap energy, and that the A-site has effects the stability and optical qualities, as previously discussed. Zhenyue Wu *et al.* used the halogen substitution strategy to increase the Curie temperature (T_c) by 85.2 K of (3-bromopropylaminium)$_2$(formamidinium)Pb_2Br_7 when we compared it to the prototypical compound (*n*-propylaminium)$_2$(formamidinium)Pb_2Br_7.[22] Moreover, the halogen substitution on the organic cation can narrow down the gap energy of $(CH_3CH_2NH_3)_3BiBr_6$ with a phase transition of 243 K, and a band gap of 2.36 eV undergoes a decrease in the gap energy and an increase in the phase transition, when it had a substitution of hydrogen by chloride atoms in the A-site.[23] However, controlling the physical properties such as Curie temperature and optical band gaps is still a challenge for researchers.[24] Fortunately, the capacity to modify molecular configurations to modulate the basic characteristics of materials provides a rich platform for the design of optical, phase-change, luminescence, and ferroelectric materials.[25–29] To the moment, lead continues to yield the finest outcomes for hybrid perovskites, which are the most studied ones compared to other metals. This fact presents a drawback to the hybrid perovskite industry and the application of these materials in some fields due to the high toxicity of lead.[30] This problem shifts the research focus to lead-free hybrid perovskites as a promising solution. To solve the toxicity issue, a lot of research studies concentrate on lead-free metals such as Sn, Ge, Cu, and Bi.[31–36] Despite their advantages, hybrid halide bismuthates of $A_3Bi_2X_9$ materials remain relatively underexplored. In this context, designing new non-centrosymmetric lead-free hybrid compounds will open extensive perspectives for optoelectronic applications. Focusing on enhancing Bi-based hybrid perovskite performance, we used the halogen substitution in the A-site to get better properties. In this work, we combined several experimental techniques to characterize the structural, electrical, optical, and photoluminescence properties of a novel bismuth-based perovskite-like compound, $(BrC_5H_{13}N)_3Bi_2Br_9$.

Experimental synthesis and characterization

Reagents and materials

All reagents were used without any purification. $BrCH_2CH_2N(CH_3)_3\cdot Br$ ((2-bromoethyl)trimethylammonium bromide, 98%, Sigma-Aldrich), Bi_2O_3 (bismuth(III) oxide, 99%, Sigma-Aldrich), HBr (hydrobromic acid, 48% in water, Sigma-Aldrich), and ethanol anhydrous (analytical grade, Sinopharm Chemical Reagent Co., Ltd, China).

Synthesis of $(BrC_5H_{13}N)_3Bi_2Br_9$

(2-Bromoethyl)trimethylammonium bromide (0.740 g, 3 mmol) was added to 20 mL of ethanol and stirred. This solution was carefully layered over an aqueous solution of hydrobromic acid (5 mL) containing 0.465 g of Bi_2O_3. The mixture was stirred for 30 minutes, and the resulting yellow precipitate was collected by filtration. Yellow crystals of $(BrC_5H_{13}N)_3Bi_2Br_9$ suitable for single-crystal X-ray diffraction analysis were obtained after 3 days. Yield: 82%. The single crystals were characterized by elemental analysis: C, 11.21% (theor. 11%); H, 2.52% (theor. 2.4%); N, 2.43% (theor. 2.56%); Br, 56.24% (theor. 58.53%).

Chemical characterization

IR absorption spectrum of the crystallized powders in KBr was recorded using a PerkinElmer FT-IR 1000 spectrometer in the 400–4000 cm^{-1} range. IR-spectrum at room temperature confirms the formation of the entitled compound (Fig. S1†). The assignments of the most relevant modes associated with vibrations of $(BrC_5H_{13}N)_3Bi_2Br_9$ are mentioned in Table S1.†

Differential Scanning Calorimetry (DSC) measurements were recorded with raw powders using a NETZCSCH DSC 200 F3 instrument (Pt crucibles and Al_2O_3 as a reference). A powder sample with a mass of about 10 mg was weighed. The DSC were conducted at a heating-cooling rate of 5 K min^{-1} in the range of 25–180 °C under a nitrogen atmosphere.

Thermogravimetric analysis (TGA) was performed using a Setaram SETSYS 16/18 instrument in the temperature range of 296–700 K at a ramp rate of 5 K min^{-1}.

Optical absorption was performed using a UV-vis Lambda9 spectrometer. The optical band gap was estimated by Tauc plots using solid-state absorption spectra and the direct band gap approximation. Photoluminescence (PL) spectra were obtained using a NanoLog composed of an iH320 spectrograph equipped

with a Synapse QExtra charge-coupled device by excitation with a monochromated 450 W Xe lamp. Fluorescence microscopic images were acquired using a Nikon Eclipse TE2000-U inverted confocal microscope equipped with a Linkam LTS420 cooling system by excitation with a 100 W Hg lamp with a 330–380 nm band-pass excitation filter.

Using a SOLARTRON SI 1260 impedance device connected to a dielectric interface at temperatures between 303 and 423 K, the electrical measurements of the real and imaginary components of the impedance parameters (Z' and Z'') were performed on pellet disks. After grinding single crystals in an agate mortar, a pellet was formed with a diameter of 8 mm and a thickness of 1 mm using a pellet mold with 8 mm diameter and 5 tons of pressure per millimeter. On the surfaces of this pellet, we deposited a layer of silver lacquer to ensure good contact with the copper electrodes. The measurements were made in the frequency range of 1–10^6 Hz. The pellet's surfaces were coated with an 8 mm-diameter circular copper electrode.

Single-crystal X-ray diffraction

Single-crystal X-ray diffraction data of $(BrC_5H_{13}N)_3Bi_2Br_9$ were collected at T = 295 K, using a Rigaku Oxford Diffraction diffractometer equipped with an Atlas CCD detector and micro-focus Cu-Kα radiation (λ = 1.54184 Å). Intensities were corrected for Lorentz-polarization effects, as well as for absorption effects (Gaussian method using the CrysAlisPro program, Rigaku Oxford Diffraction, V1.171.40.45a, 2019). The structures were solved using the SHELXT program and refined by full-matrix least-squares routines against F^2 using the SHELX program (G. M. Sheldrick-2018, SHELXT-2018/2 and SHELXL-2018/3)[37,38] through the WinGX program suite.[39] H-atoms were positioned geometrically. The compound $(BrC_5H_{13}N)_3Bi_2Br_9$ exhibits disorders associated with carbon and hydrogen atoms among (2-bromoethyl)trimethylammonium organic cations. The C11, C12, H11 and H12 atoms are split in two positions with 47% and 53% atomic site occupancies. A summary of crystallographic data and refinement results are listed in Table S2.† The relevant selected bond lengths and angles are listed in Tables S3–S5.† A complete list of crystallographic data, along with the atomic coordinates, the anisotropic displacement parameters and bond distances and angles are given as a CIF file (CCDC number 2429859). Structural illustrations were generated using the Diamond software.[40]

Results and discussion

Structural aspects

Yellow prismatic crystals of $(BrC_5H_{13}N)_3Bi_2Br_9$ were obtained by adding Bi_2O_3 in HBr to an ethanol solution containing (2-bromoethyl)trimethylammonium bromide. Structural analysis performed by single-crystal X-ray diffraction revealed that the compound crystallizes in the non-centrosymmetric $P2_12_12_1$ space group at room temperature (Table S2†).

The asymmetric unit of the compound $(BrC_5H_{13}N)_3Bi_2Br_9$ consists of three organic ammonium cations and one $[Bi_2Br_9]^{3-}$ anion (Fig. 1(a)). The Bi(III) ions are located in a hexa-coordinated environment, giving rise to a discrete perovskite-type. Fig. 1(b)

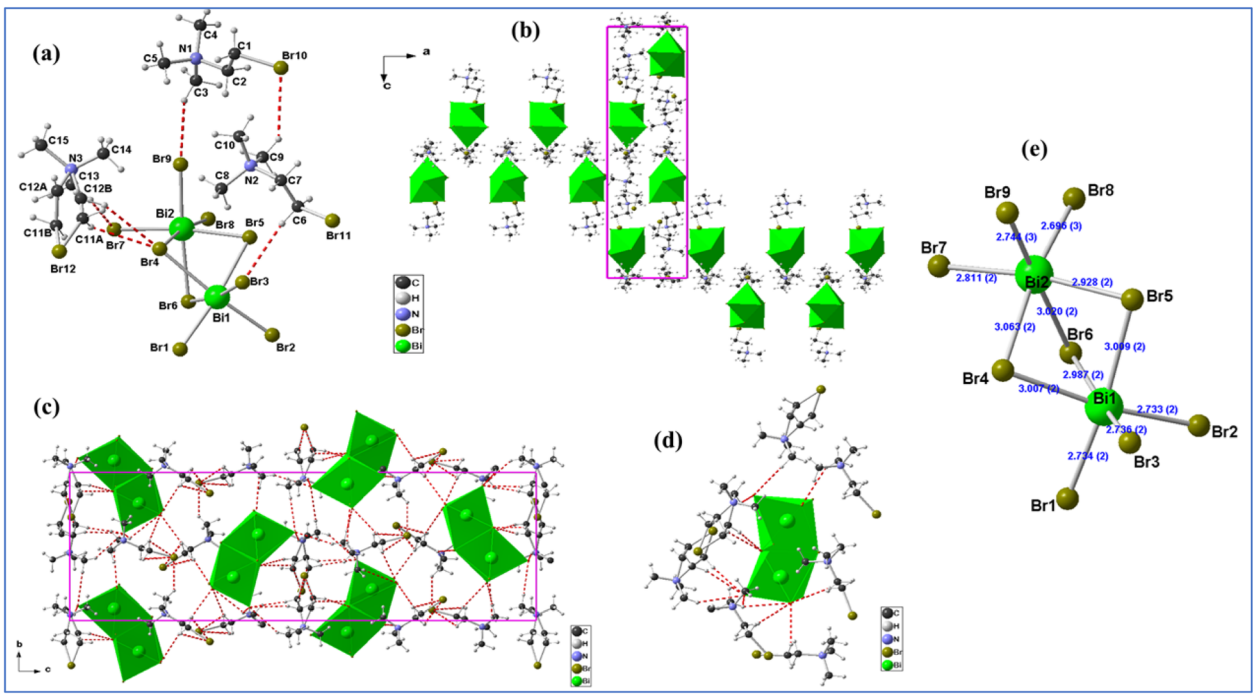

Fig. 1 (a) Asymmetric unit of $(BrC_5H_{13}N)_3Bi_2Br_9$. (b) General view along the b direction showing $[BrC_5H_{13}N]^+$ cations localized in the inner cavity of the perovskite-like sheet and in the interlayer space. (c) C–H···Br H-bonding interactions present in $(BrC_5H_{13}N)_3Bi_2Br_9$ (red dashed lines: H···Br contacts <3.14 Å). (d) Neighboring (2-bromoethyl)trimethylammonium cations in the environment of bi-octahedral $[Bi_2Br_9]^{3-}$ anions. ® Bi-octahedral Bi_2Br_9 unit with Bi and Br bond distances.

shows a projection of the structure of $(BrC_5H_{13}N)_3Bi_2Br_9$ in the (*a*, *c*) plane. The anionic network is formed by clusters $[Bi_2Br_9]^{3-}$ separated by organic cations $(BrC_5H_{13}N)^+$. Consequently, (2-bromoethyl)trimethylammonium cations are localized in the interlayer space, leading to a more appropriate structural formula of $(BrC_5H_{13}N)_3Bi_2Br_9$. This structure is analogous to that of hybrid perovskites. The cohesion between these different entities is ensured by hydrogen bonding (C–H···Br) interactions. This arrangement is similar to the one found in the structures of bismuth(III)-halide perovskites such as $[(CH_3)_3S]_3[Bi_2Br_9]$ and $(CH_3NH_3)_3(Bi_2I_9)$.[41,42] The incorporation of a larger organic cation restrained the formation of a polymeric configuration for the halogenobismuthate(III) complexes, as found in the previously reported structures of $[Bi_2Br_9]^{3-}$ with other ammonium cations.[43] In the bimetallic $[Bi_2Br_9]^{3-}$ ion, three Br-atoms bridge two Bi-centers, with Bi–Br–Bi angles varying from 81.21(6)° and 83.41(5)° and Bi–Br bond lengths between 2.928(2) Å and 3.063(2) Å, which are considerably longer than the terminal Bi–Br bonds (2.696(3) Å to 2.811(2) Å) (Fig. 1(e)). The observed variations in the bond lengths of $(BrC_5H_{13}N)_3Bi_2Br_9$ are comparable with the already described structurally similar Bi(III) hybrid compounds[44] (see Tables S3–S4†). In addition, the organic cation $(BrC_5H_{13}N)^+$ bonds and angles show that C–C, C–N, and C–Br bonds are, respectively, between (1.44 Å and 1.53 Å), (1.44 Å and 1.54 Å), and (1.92 Å and 2.05 Å) while the angles C–C–Br, C–C–N, N–C–C, and C–N–C vary, respectively, from 96 to 108°, 102 to 113°, 109 to 114°, and 92 to 131°. These results are comparable to those observed in the structures of $[(CH_3)_3N(CH_2)_2Br]_2[CoBr_4]$ and $[(CH_3)_3N(CH_2)_3Br]_2PdBr_4$.[45] It is interesting to note that some carbon and hydrogen atoms occupy two equivalent locations, with atomic occupancies of 0.47 : 0.53, in the organic cations. The H-bonding interactions present in the compound revealed that each $[Bi_2Br_9]^{3-}$ unit is connected to seven ammonium units through H-bonding interactions (Fig. 1(d)). Indeed, the $-CH_3$ and $-CH_2$-hydrogen atoms of these bridging ammonium cations are H-bonded to both terminal and bridging $[Bi_2Br_9]^{3-}$ anions, with C–H···Br bond lengths ranging from 3.48 (3) Å to 4.04 (3) Å, while the C–H···Br angles range between 113° and 172°. These interactions form a 3D H-bonded network extending along the *bc*-plane (Fig. 1(c)).

Thermal decomposition

TGA and DSC measurements were carried out to highlight the phase transitions and the thermal stability of the $(BrC_5H_{13}N)_3Bi_2Br_9$ compound. The curves obtained during the decomposition of $(BrC_5H_{13}N)_3Bi_2Br_9$, under flowing air at a heating rate of 5 °C min^{-1} between 296 and 700 K are reported in Fig. S2(a).† The results showed that $(BrC_5H_{13}N)_3Bi_2Br_9$ suffered from weight loss twice. The slow and slight mass decrement (3%) observed on TG at 310 K is connected with the removal of hygroscopic water. The weight loss, between 425 and 480 K, can be attributed to the decomposition of the organic cations together with the bromide removed to support the charge neutrality and corresponding to the formation of Bi_2Br_6 (observed weight loss: 46.9%; theoretical: 45.22%).

The DSC measurements showed an endothermic peak located at 320 K. For this compound, no phase transition can be identified (see Fig. S2(b)†).

Gap energy and AC conductivity

The fundamental processes through which light is absorbed, reflected, or transmitted by materials are crucial for understanding their electronic structures. These interactions provide key insights into the material's electronic properties such as band gaps, conduction mechanisms, and optical behaviors. In this section, we will outline and discuss the $(BrC_5H_{13}N)_3Bi_2Br_9$ compound's basic optical properties in order to evaluate its quality and light efficiency. The sample's experimental UV-vis absorbance spectrum, measured at room temperature and in the wavelength range of 200–800 nm, is shown in Fig. 2(a). Significant ultraviolet domain absorption is clearly present in this spectrum, suggesting that it is a fundamental band characteristic.

An inter-band transition between parabolic bands must produce the absorption edge in a Tauc plot. This approach is not appropriate for materials with strong band tails overlapping the fundamental absorbance, such as 2D, 1D, or 0D systems.[46] Because of its low-dimensional structure,[47] $(BrC_5H_{13}N)_3Bi_2Br_9$ can be used to determine its band gap using the Tauc plot method, which is best suited for powder compounds and is provided by this equation:

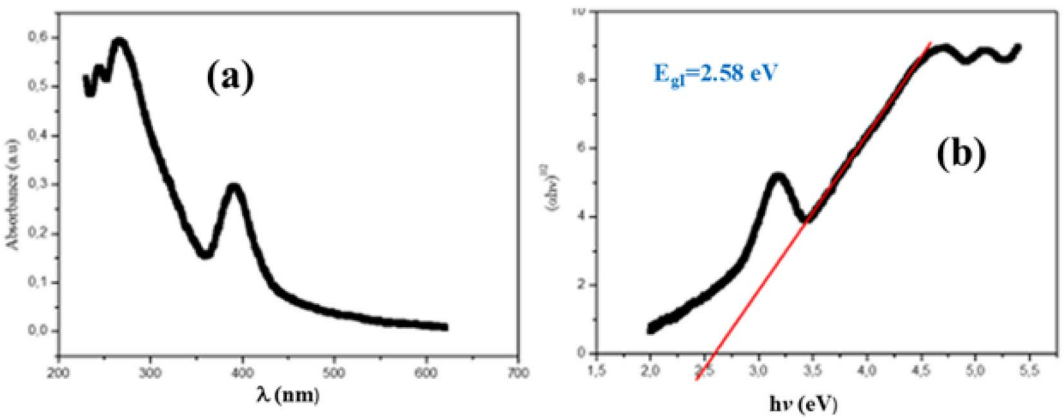

Fig. 2 (a) Variation in absorbance with the wavelength of $(BrC_5H_{13}N)_3Bi_2Br_9$. (b) Gap energy of $(BrC_5H_{13}N)_3Bi_2Br_9$.

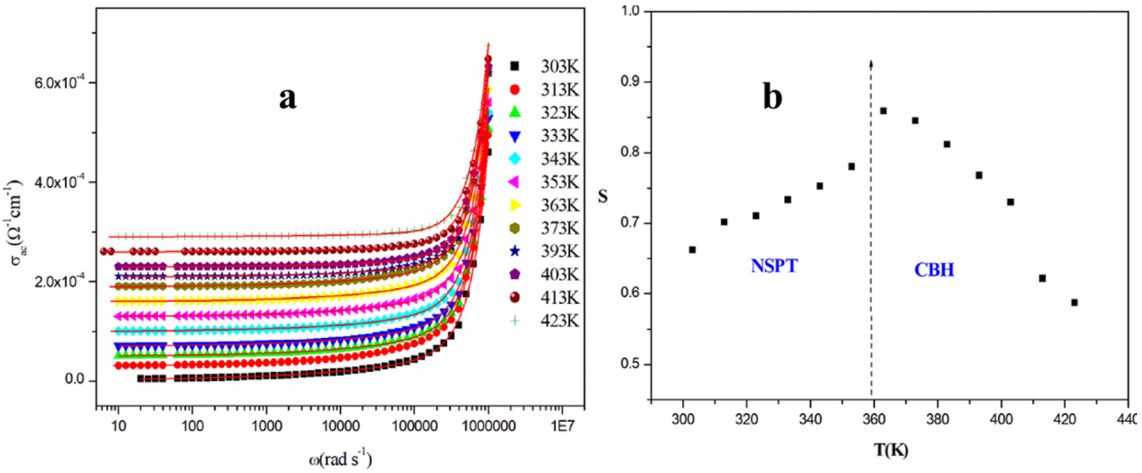

Fig. 3 (a) Frequency dependence of the AC conductivity at different temperatures for $(BrC_5H_{13}N)_3Bi_2Br_9$. (b) Variations in universal exponent S as a function of temperature for $(BrC_5H_{13}N)_3Bi_2Br_9$.

$$(F(R))^{1/n} = B\,(h\nu - E_g) \quad (1)$$

where $F(R)$ is the Kubelka–Munk function:[48]

$$F(R) = (1 - R)^2/2R \quad (2)$$

The symbol of E_g stands for the optical band gap energy, and n is a parameter that describes the optical transition's nature between the valence band and the conduction band. The value of n indicates the nature of the transition: $n = 2$ for indirect permitted transitions $\frac{1}{2}$ and $n = 1/2$ for direct permitted transitions. Based on the report in the literature and similar compounds, both the conduction band minimum (CB_{Min}) and the valence band maximum (VB_{Max}) are localized at different positions in the Brillouin zone, which should be reminiscent of the indirect feature of the band gap. The (CB_{Min}) are mainly from the unoccupied Bi-6p orbitals, and nonbonding states of Br-4p form the bands at the (VB_{Max}). Obviously, both the VB_{Max} and the CB_{Min} originate from the electronic states of Bi and Br atoms, and hence, it is the inorganic $[Bi_2Br_9]$ framework that determines the bandgap of the material.[42]

Fig. 2(b) displays the plot of $(F(R))^{1/2}$ *versus* photon energy ($h\nu$), which can be used to determine the indirect band gap energy. The estimated band gap energy from the intercept of the tangent to the plot is 2.58 eV, which is analogous to materials based on Bi(III).[42] This result indicates that our material is a semiconductor and a potential optoelectronic candidate.

To confirm the semiconductor character of $(BrC_5H_{13}N)_3Bi_2Br_9$ materials, we studied the AC conductivity at different frequencies and temperatures, which are also used to distinguish the conduction type and provide information about conduction modes. The electrical conductivity *vs.* angular frequency at different temperatures is given in Fig. 3(a) using a log–log scale. The frequency behaviour of conductivity is split into two regions. As the frequency increases, the first region at low and medium frequencies corresponds to the grain boundary effect and the second region at high frequencies suggests the grain effect. The high electrical conductivity σ_{ac} values reach around 2×10^{-4} to 5×10^{-4} Ω cm^{-1}, which is in great agreement with 3.8 10^2 S m^{-1} and confirms the semiconductor character of this material. These spectra are described by Jonscher's universal power law, which show two regions:[49]

$$\sigma_{ac} = \sigma_{dc} + A \times \omega^S \quad (3)$$

where σ_{dc} represents the conductivity in direct current, A is the specific temperature-dependent constant that determines the polarizability force and S is the power law exponent, which provides valuable insights into the underlying conduction models. Fig. 3(b) records the variation in the exponent S with temperature. According to Elliot's hypothesis,[50,51] we can use this variation, which translates the interaction between mobile ions and their surroundings, to discover the mechanisms of conduction in the $(BrC_5H_{13}N)_3Bi_2Br_9$ compound.

It may be observed that as the temperature rises, the evolution of the exponent (S) increases in the first phase and decreases in the second phase. This finding implies that the non-overlapping small polaron tunneling (NSPT) model and the correlated barrier hopping (CBH) model can be described as the electrical conduction in the two phases, respectively.

Impedance spectroscopy and conductivity of grain

The complex impedance spectroscopy provides information on various microstructure characteristics of materials, including the grain, electrode interfaces, and grain boundaries. It demonstrates a clear relationship between the response of the actual system and the ideal circuit produced by the electrical components. Complex impedance plots for a range of frequencies and temperatures are shown in Fig. 4(a). Two depressed semicircles with centers moved down toward the real axis are visible in the $-Z''$ *vs.* Z' plots, indicating a non-Debye relaxation in the material's electrical processes. These semicircles are attributed to the grain (at higher frequencies) and grain boundary response in this material.

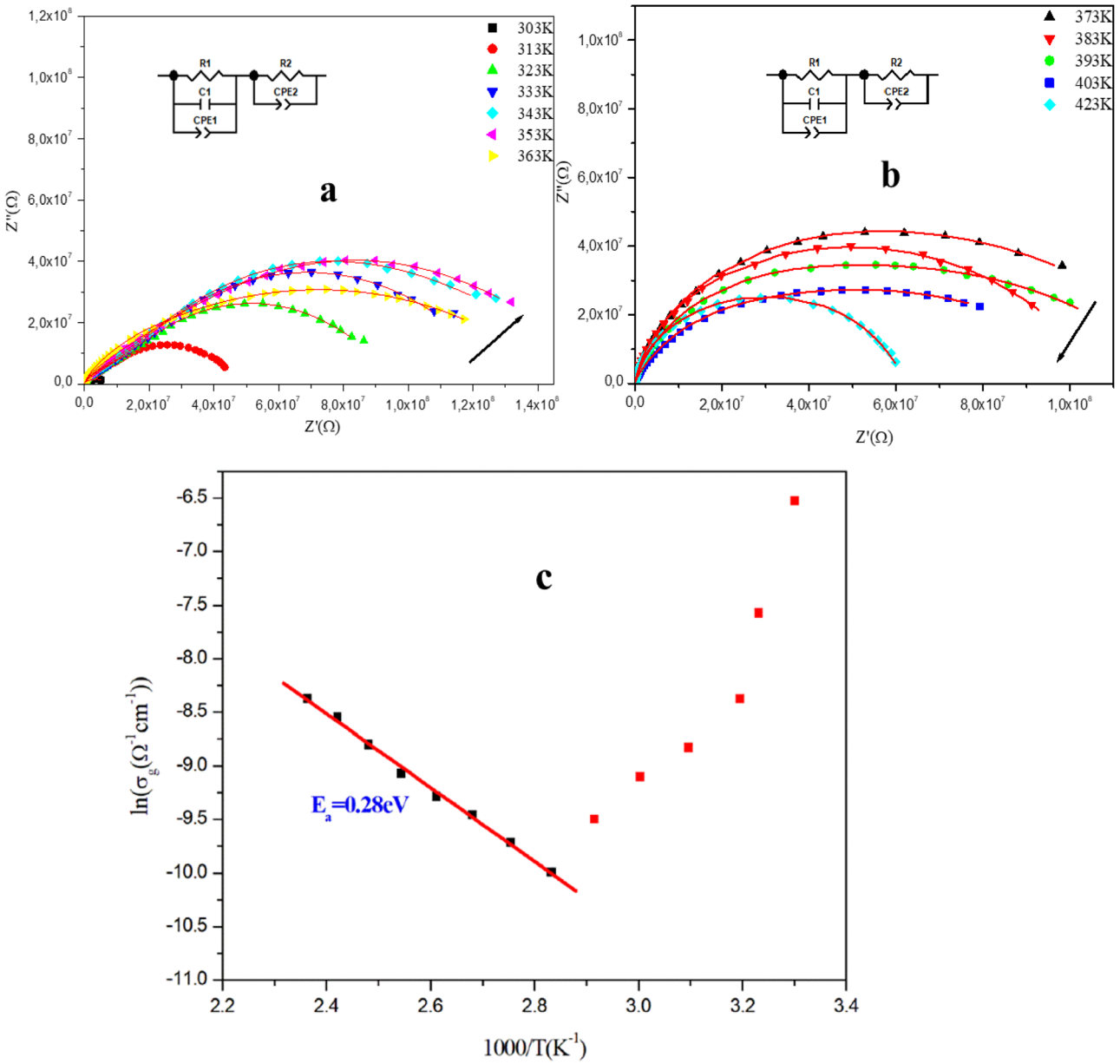

Fig. 4 Complex impedance spectra and equivalent circuit of the $(BrC_5H_{13}N)_3Bi_2Br_9$ compound at different temperatures (a) between 303 K and 363 K and (b) between 373 K and 423 K, and (c) variations in $\ln(\sigma_g)$ *versus* $1000/T$ for the $(BrC_5H_{13}N)_3Bi_2Br_9$ compound.

Two distinct regions are seen. The first is between 303 and 363 K, where arc circles are visible in the complex plane plots and grow larger as the temperature rises. This phenomenon is due to the evaporation of adsorbed H_2O molecules on the material surface. Due to overlapping grain response and grain boundaries, the second region, which is between 373 K and 423 K, shows wide and deformed semi-circles. The semiconductor nature and a thermally activated conductivity mechanism are indicated by the semicircles' decreasing radius as the temperature rises. Using the Z-View software, we have tried to identify an equivalent circuit that describes the behavior of this material (inset Fig. 4(a) and (b)) and that enables the separation of the grain and grain boundary response.

The conductivity of the grain (σ_g) may be determined using the following formula, based on the resistance values determined from the equivalent circuit:[52]

$$\sigma_g = \frac{e}{R_1 S} \quad (4)$$

where R_1 is the resistance ascertained from the equivalent circuit, S is the pellet's surface area, and e is the pellet's thickness.

Temperature dependence of σ_g is shown in Fig. 4(c). This variation is well described by the Arrhenius law only after 363 K, which confirms the H_2O release effect. The activation energy of the phase after 363 K is equal to $E_a = 0.28$ eV. This value

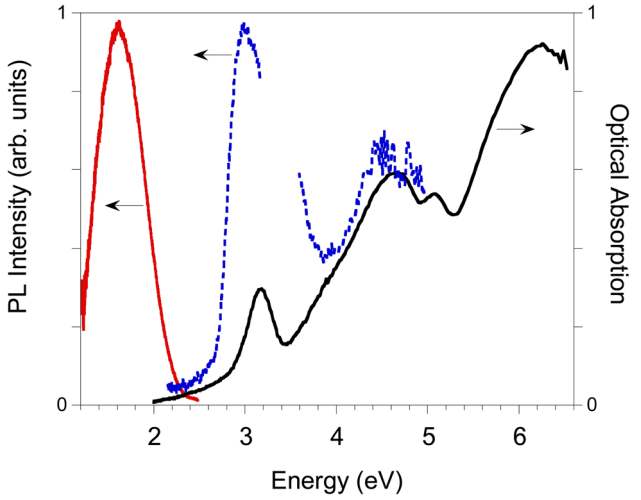

Fig. 5 Normalized optical absorption spectra of the $(BrC_5H_{13}N)_3Bi_2Br_9$ cast film (solid black line) and photoluminescence spectra of $(BrC_5H_{13}N)_3Bi_2Br_9$ crystals (solid red line, photoluminescence excited at 3.26 eV; blue dashed line, excitation-dependent photoluminescence intensity monitored at 1.70 eV).

indicates that this material may exhibit a combination of ionic and electronic conduction.

Photoluminescence properties of $(BrC_5H_{13}N)_3Bi_2Br_9$

The photoluminescence properties of $(BrC_5H_{13}N)_3Bi_2Br_9$ crystalline powders are reported in Fig. 5. The morphology in the crystals were confirmed by optical polarizing microscopy (Fig. S3†). The photoluminescence spectrum exhibits a broad and weak band in the near-infrared (NIR) region, centered around 1.7 eV, which is likely attributed to self-trapped states. Its excitation profile displays a narrow peak at 3.0 eV (blue dashed line in Fig. 5) in agreement with the absorption spectrum of the cast film, that reveals the main peaks at 3.16 eV and 4.66 eV (black solid line in Fig. 5). The emission of the film is weak showing the broad band emission at 1.69 eV with an additional narrow component at 2.87 eV, resembling excitonic emission (Fig. S4†). Although the photoluminescence intensity is relatively weak, the position of its main emission, close to the NIR region, coupled with the significant Stokes shift (1.46 eV) between absorption and emission, presents intriguing possibilities for optoelectronic applications, where such properties can be leveraged to develop advanced devices for light detection, energy conversion, or communication technologies.

Conclusion

In conclusion, we successfully synthesized a new Bi-based, eco-friendly organic–inorganic hybrid perovskite-like compound, $(BrC_5H_{13}N)_3Bi_2Br_9$. This material represents a promising addition to the field of hybrid perovskites due to its unique structural and electronic properties. The compound is non-centrosymmetric, crystallizing in the orthorhombic space group $P2_12_12_1$, and features an indirect bandgap energy of 2.58 eV. Its broad band emission, which is close to the NIR region, coupled with its very large Stokes shift, highlights its potential for optoelectronic applications. The electrical study shows a high value of conductivity and confirms the gap energy, which indicates the semiconductor character of this material. The equivalent circuit has been chosen and indicates the contribution of the grain and grain boundary in the conduction. The activation energy suggests the combination of ionic and electronic conduction.

Data availability

The raw/processed data required to reproduce these findings are available and can be sent if requested.

Author contributions

The manuscript was written through contributions from all the authors. All authors have given approval to the final version of the manuscript. Yassine Ben Elhaj: conceptualization, methodology, investigation, data curation, writing – original draft, review & editing. Fadhel Hajlaoui: conceptualization, methodology, investigation, data curation, supervision, writing – original draft, review & editing. Karim Karoui: methodology, investigation, data curation, supervision, writing – original draft, review & editing. Erika Kozma: data curation, writing – review & editing, funding acquisition. Chiara Botta: investigation, data curation, writing – review & editing, funding acquisition. Nabil Zouari: investigation, data curation, writing – review & editing, funding acquisition. Magali Allain: investigation, data curation, writing – review & editing Nicolas Mercier: investigation, data curation, writing – review & editing.

Conflicts of interest

There are no conflicts to declare.

Acknowledgements

The authors thank the University of Sfax and the University of Angers for X-ray diffraction data collection. The authors acknowledge financial support from the National Research Council of Italy (CNR) and the Ministry of Higher Education and Scientific Research of Republic of Tunisia (MHESR) under the Bilateral Joint Program, “Lead-free perovskite nanocrystals embedded in polymeric electrospun nanofibers for fluorescent sensors (LEAF) 2023–2024”, grant agreement no. 23/TI 1101.

References

1 Q. Tai, P. You, H. Sang, Z. Liu, C. Hu, H. L. W. Chan and F. Yan, Efficient and stable perovskite solar cells prepared in ambient air irrespective of the humidity, *Nat. Commun.*, 2016, 7, 11105, DOI: 10.1038/ncomms11105.
2 K. Lin, J. Xing, L. N. Quan, F. P. G. de Arquer, X. Gong, J. Lu, L. Xie, W. Zhao, D. Zhang, C. Yan, W. Li, X. Liu, Y. Lu, J. Kirman, E. H. Sargent, Q. Xiong and Z. Wei, Perovskite light-emitting diodes with external quantum efficiency

exceeding 20 per cent, *Nat*, 2018, **562**, 245–248, DOI: 10.1038/s41586-018-0575-3.

3 X. Fu, S. Jiao, N. Dong, G. Lian, T. Zhao, S. Lv, Q. Wang and D. Cui, A $CH_3NH_3PbI_3$ film for a room-temperature NO2 gas sensor with quick response and high selectivity, *RSC Adv.*, 2018, **8**, 390–395, DOI: 10.1039/C7RA11149E.

4 Y. Liu, Y. Liu and Y. Guo, Organic–inorganic hybrid perovskite materials and their application in transistors, *Mater. Chem. Front.*, 2023, **7**, 5215–5246, DOI: 10.1039/D3QM00697B.

5 S. Han, X. Liu, Y. Liu, Z. Xu, Y. Li, M. Hong, J. Luo and Z. Sun, High-Temperature Antiferroelectric of Lead Iodide Hybrid Perovskites, *J. Am. Chem. Soc.*, 2019, **141**, 12470–12474, DOI: 10.1021/jacs.9b05124.

6 L. Mao, C. C. Stoumpos and M. G. Kanatzidis, Two-Dimensional Hybrid Halide Perovskites: Principles and Promises, *Am. Chem. Soc.*, 2019, **141**, 1171–1190, DOI: 10.1021/jacs.8b10851.

7 N. Mercier, Hybrid Halide Perovskites: Discussions on Terminology and Materials, *Angew. Chem., Int. Ed.*, 2019, **58**, 17912–17917, DOI: 10.1002/anie.201909601.

8 H. Min, D. Y. Lee, J. Kim, G. Kim, K. S. Lee, J. Kim, M. J. Paik, Y. K. Kim, K. S. Kim, M. G. Kim, T. J. Shin and S. I. Seok, Perovskite solar cells with atomically coherent interlayers on SnO2 electrodes, *Nature*, 2021, **598**, 444–450, DOI: 10.1038/s41586-021-03964-8.

9 J. S. Kim, J. M. Heo, G. S. Park, S. J. Woo, C. Cho, H. J. Yun, D. H. Kim, J. Park, S. C. Lee, S. H. Park, E. Yoon, N. C. Greenham and T. W. Lee, Ultra-bright, efficient and stable perovskite light-emitting diodes, *Nature*, 2022, **611**, 688–694, DOI: 10.1038/s41586-022-05304-w.

10 A. Maity, A. K. Raychaudhuri and B. Ghosh, High sensitivity NH3 gas sensor with electrical readout made on paper with perovskite halide as sensor material, *Sci. Rep.*, 2019, **9**, 7777, DOI: 10.1038/s41598-019-43961-6.

11 H. Lin, C. Zhou, Y. Tian, T. Siegrist and B. Ma, Low-Dimensional Organometal Halide Perovskites, *ACS Energy Lett.*, 2018, **3**, 54–62, DOI: 10.1021/acsenergylett.7b00926.

12 A. Mitrofanov, Y. Berencén, E. Sadrollahi, R. Boldt, D. Bodesheim, H. Weiske, F. Fabian Paulus, J. Geck, G. Cuniberti, A. Kuc and B. Voit, Molecular engineering of naphthalene spacers in low-dimensional perovskites, *J. Mater. Chem. C*, 2023, **11**, 5024–5031, DOI: 10.1039/D3TC00132F.

13 Y. Zou, Y. Gao and Y. Liu, The role of organic spacers in 2D/3D hybrid perovskite solar cells, *Mater. Chem. Front.*, 2024, **8**, 82–103, DOI: 10.1039/D3QM00726J.

14 L. Zhang, M. Xia, Y. Zhang, L. Song, X. Guo, Y. Zhang, Y. Wang and Y. Xia, he Effect of Organic Spacer Cations with Different Chain Lengths on Quasi-Two-Dimensional Perovskite Properties, *Inorganics*, 2024, **12**, 1–11, DOI: 10.3390/inorganics12010012.

15 E. Mahal, S. Charan Mandal and B. Pathak, Understanding the role of spacer cation in 2D layered halide perovskites to achieve stable perovskite solar cells, *Adv. Mater.*, 2022, **3**, 2464–2474, DOI: 10.1039/D1MA01135A.

16 C. Tablero Crespo, The effect of the halide anion on the optical properties of lead halide perovskites, *Sol. Energy Mater. Sol. Cells*, 2019, **195**, 269–273, DOI: 10.1016/j.solmat.2019.03.023.

17 K. T. Butler and J. Mater, The chemical forces underlying octahedral tilting in halide perovskites, *J. Chem. C*, 2018, **6**, 12045–12051, DOI: 10.1039/C8TC02976H.

18 H. L. B. Boström, J. A. Hilla and A. L. Goodwin, Columnar shifts as symmetry-breaking degrees of freedom in molecular perovskites, *Phys. Chem. Chem. Phys.*, 2016, **18**, 31881–31894, DOI: 10.1039/C6CP05730F.

19 H. L. B. Boström, M. S. Senn and A. L. Goodwin, Recipes for improper ferroelectricity in molecular perovskites, *Nat. Commun.*, 2018, **9**, 2380, DOI: 10.1038/s41467-018-04764-x.

20 B. Dridi Rezgui, I. Touhami, F. Khan, K. B. Messaoud, C. B. Alaya, Z. Antar and M. Bouaïcha, Cation substitution-induced band gap and stability engineering of formamidinium-based perovskite films prepared in ambient conditions, *Opt. Mater.*, 2023, **135**, 113267, DOI: 10.1016/j.optmat.2022.113267.

21 Z. Li, M. Yang, J.-S. Park, S.-H. Wei, J. J. Berry and K. Zhu, Stabilizing Perovskite Structures by Tuning Tolerance Factor: Formation of Formamidinium and Cesium Lead Iodide Solid-State Alloys, *Chem. Mater.*, 2016, **28**(1), 284–292, DOI: 10.1021/acs.chemmater.5b04107.

22 Z. Wu, W. Zhang, H. Ye, Y. Yao, X. Liu, L. Li, C. Ji and J. Luo, Bromine-Substitution-Induced High-Tc Two-Dimensional Bilayered Perovskite Photoferroelectric, *J. Am. Chem. Soc.*, 2021, **143**(20), 7593–7598, DOI: 10.1021/jacs.1c00459.

23 H. H. Li, C. F. Wang, Y. X. Wu, F. Jiang, C. Shi, H. Y. Ye and Y. Zhang, Halogen substitution regulates the phase transition temperature and band gap of semiconductor compounds, *Chem. Commun.*, 2020, **56**, 1697–1700, DOI: 10.1039/C9CC09477F.

24 K. Trabelsi, N. Drissi, F. Hajlaoui, M. Zighrioui, A. Rhaiem, N. Audebrand, T. Roisnel and K. Karim, $[(CH_3)_2NH_2]_2PdBr_4$, a layered hybrid halide perovskite semiconductor with improved optical and electrical properties, *RSC Adv.*, 2023, **13**, 23348–23358, DOI: 10.1039/D3RA04085B.

25 N. Song, S.-P. Chen, X.-W. Fan, Y.-H. Tan, W.-J. Wei and Y.-Z. Tang, Regulating Reversible Phase Transition Behaviors by Poly-H/F Substitution in Hybrid Perovskite-Like $2[CH_2FCH_2NH_3]\cdot[CdCl_4]$, *ACS Omega*, 2020, **5**(12), 6773–6780, DOI: 10.1021/acsomega.0c00113.

26 C. Han, A. J. Bradford, J. A. McNulty, W. Zhang, P. Shiv Halasyamani, A. M. Z. Slawin, F. D. Morrison, S. L. Lee and P. Lightfoot, Polarity and Ferromagnetism in Two-Dimensional Hybrid Copper Perovskites with Chlorinated Aromatic Spacers, *Chem. Mater.*, 2022, **34**, 2458–2467, DOI: 10.1021/acs.chemmater.2c00107.

27 F. Hleli, N. Mercier, M. Ben Haj Salah, M. Allain, T. Travers, D. Gindre, N. Zouari and C. Botta, Morphology and temperature dependence of a dual excitonic emissive 2D bromoplumbate hybrid perovskite: the key role of crystal edges, *J. Mater. Chem. C*, 2022, **10**, 10284–10291, DOI: 10.1039/D2TC01449A.

28 Y. Sui, Y.-S. Zhong, J.-J. Wang, Q. Xia, L.-J. Wang and D.-S. Liu, A semiconducting organic–inorganic hybrid ($[BrCH_2CH_2N(CH_3)_3]^{2+}[CuBr_4]^{2-}$) with switchable dielectric properties derived from an unusual piston-like displacive movement, *J. Mater. Chem. C*, 2019, **7**, 14294–14300, DOI: **10.1039/C9TC05328J**.

29 Y. Ai, X.-G. Chen, P.-P. Shi, Y.-Y. Tang, P.-F. Li, W.-Q. Liao and R.-G. Xiong, Fluorine Substitution Induced High Tc of Enantiomeric Perovskite Ferroelectrics: (R)- and (S)-3-(Fluoropyrrolidinium)$MnCl_3$, *J. Am. Chem. Soc.*, 2019, **141**, 4474–4479, DOI: **10.1021/jacs.9b00886**.

30 N. K. Noel, S. D. Stranks, A. Abate, C. Wehrenfennig, S. Guarnera, A.-A. Haghighirad, A. Sadhanala, G. E. Eperon, S. K. Pathak, M. B. Johnston, A. Petrozza, L. M. Herz and H. J. Snaith, Lead-free organic–inorganic tin halide perovskites for photovoltaic applications, *Energy Environ. Sci.*, 2014, **7**, 3061–3068, DOI: **10.1039/C4EE01076K**.

31 J. Cao and F. Yan, Recent progress in tin-based perovskite solar cells, *Energy Environ. Sci.*, 2021, **14**, 1286–1325, DOI: **10.1039/D0EE04007J**.

32 N. Lakhdar and A. Hima, Electron transport material effect on performance of perovskite solar cells based on $CH_3NH_3GeI_3$, *Opt. Mater.*, 2020, **99**, 109517, DOI: **10.1016/j.optmat.2019.109517**.

33 A. M. Elseman, A. E. Shalan, S. Sajid, M. M. Rashad, A. M. Hassan and M. Li, Copper-Substituted Lead Perovskite Materials Constructed with Different Halides for Working (CH3NH3)2CuX4-Based Perovskite Solar Cells from Experimental and Theoretical View, *ACS Appl. Mater. Interfaces*, 2018, **10**(14), 11699–11707, DOI: **10.1021/acsami.8b00495**.

34 T. Ngulezhu, A. S. Abdulkarim, S. Rawat, R. C. Singh, P. K. Singh, D. Singh, K. Strzałkowski and M. Srivastava, table lead free perovskite solar cells based on bismuth doped perovskite materials, *Chem. Phys. Impact.*, 2024, **9**, 100689, DOI: **10.1016/j.chphi.2024.100689**.

35 M. S. Ozório, W. X. C. Oliveira, J. F. R. V. Silveira, A. F. Nogueira and J. L. F. Da Silva, Novel zero-dimensional lead-free bismuth-based perovskites: from synthesis to structural and optoelectronic characterization, *Adv. Mater.*, 2020, **1**, 3439–3448, DOI: **10.1039/D0MA00791A**.

36 Y. Sun, A. J. Fernández-Carrión, Y. Liu, C. Yin, X. Ming, B.-M. Liu, J. Wang, H. Fu, X. Kuang and X. Xing, Bismuth-Based Halide Double Perovskite Cs2LiBiCl6: Crystal Structure, Luminescence, and Stability, *Chem. Mater.*, 2021, **33**(15), 5905–5916, DOI: **10.1021/acs.chemmater.1c00854**.

37 G. M. Sheldrick, SHELXT – Integrated space-group and crystal-structure determination, *Acta Crystallogr., Sect. A*, 2015, **71**, 3–8, DOI: **10.1107/S2053273314026370**.

38 G. M. Sheldrick, Crystal Structure Refinement with SHELXL, *Acta Crystallogr., Sect. C*, 2015, **71**, 3–8, DOI: **10.1107/S2053229614024218**.

39 L. Farrugia, WinGX and ORTEP for Windows: an update, *J. Appl. Crystallogr.*, 2012, **45**, 849–854, DOI: **10.1107/S0021889812029111**.

40 K. Brandenburg and M. Berndt, *Diamond (Version 2), Crystal Impact*, Bonn, 2001.

41 K. Eckhardt, V. Bon, J. Getzschmann, J. Grothe, F. M. Wisser and S. Kaskel, Crystallographic insights into $(CH_3NH_3)_3(Bi_2I_9)$: a new lead-free hybrid organic–inorganic material as a potential absorber for photovoltaics, *Chem. Commun.*, 2016, **52**, 3058–3060, DOI: **10.1039/C5CC10455F**.

42 Y.-Z. Zhang, D.-S. Sun, J.-X. Gao, X.-N. Hua, X.-G. Chen, G.-Q. Mei and W.-Q. Liao, A Semiconducting Organic-Inorganic Hybrid Perovskite-type Non-ferroelectric Piezoelectric with Excellent Piezoelectricity, *Chem.–Asian J.*, 2019, **14**(7), 1028–1033, DOI: **10.1002/asia.201801921**.

43 N. Meena, S. Sahoo, N. Deka, V. B. Gadagin, J. K. Zareba and R. Boomishankar, Ferroelectricity and piezoelectric energy harvesting of an $A_3M_2X_9$-type 0D bromobismuthate hybrid with a bulky organic quaternary amine, *Dalton Trans.*, 2025, **54**, 2985–2990, DOI: **10.1039/D4DT03225J**.

44 R. Jakubas, M. Rok, K. Mencel, G. Bator and A. Piecha-Bisiorek, Correlation between crystal structures and polar (ferroelectric) properties of hybrids of haloantimonates(iii) and halobismuthates(iii), *Inorg. Chem. Front.*, 2020, **7**, 2107–2128, DOI: **10.1039/D0QI00265H**.

45 (*a*) I. Dakhlaoui, K. Karoui, F. Hajlaoui, N. Audebrand, T. Roisnel and F. Jomni, $[(CH_3)_3N(CH_2)_2Br]_2[CoBr_4]$ halogenometallate complex: crystal structure, high-temperature reversible phase transition, electrical and optical properties, *J. Mol. Struct.*, 2021, **1231**, 129684, DOI: **10.1016/j.molstruc.2020.129684**; (*b*) M. Saadi, I. Dakhlaoui, F. Hajlaoui, N. Drissi, M. Zighrioui, F. Jomni, N. Audebrand, M. Cordier and K. Karim, Bromination of organic spacer impacts on the structural arrangement, phase transitions, and optical and electrical properties of a hybrid halide compound: $[(CH_3)_3N(CH_2)_3Br]_2PdBr_4$, *New J. Chem.*, 2024, **48**, 182–192, DOI: **10.1039/D3NJ04819E**.

46 J. Klein, L. Kampermann, B. Mockenhaupt, M. Behrens, J. Strunk and G. Bacher, Limitations of the Tauc Plot Method, *Adv. Funct. Mater.*, 2023, **33**, 2304523, DOI: **10.1002/adfm.202304523**.

47 N. Kuganathan, A. Kordatos, N. Kelaidis and A. C. Defects, Lithium Mobility and Tetravalent Dopants in the Li_3NbO_4 Cathode Material, *Sci. Rep.*, 2019, **9**, 2192, DOI: **10.1038/s41598-018-37466-x**.

48 P. Kubelka and F. Munk, An article on optics of paint layers, *J. Tech. Phys.*, 1931, **12**, 593–601.

49 R. Murugaraj, G. Govindaraj and D. George, AC conductivity and its scaling behavior in lithium and sodium bismuthate glasses, *Mater. Lett.*, 2003, **57**, 1656–1661, DOI: **10.1016/S0167-577X(02)01047-9**.

50 S. R. Elliot, A.c. conduction in amorphous chalcogenide and pnictide semiconductors, *Adv. Phys.*, 1987, **36**, 135–217, DOI: **10.1080/00018738700101971**.

51 M. Krimi, K. Karoui, J. J. Suñol and A. B. Rhaiem, Phase transition, impedance spectroscopy and conduction mechanism of Li0.5Na1.5WO4 Material, *Phys. E*, 2018, **102**, 137–145, DOI: **10.1016/j.physe.2018.04.032**.

52 M. Petrowsky and R. Frech, Temperature Dependence of Ion Transport: The Compensated Arrhenius Equation, *J. Phys. Chem. B*, 2009, **113**, 5996–6000, DOI: **10.1021/jp810095g**.